



# Comparison of blind deconvolution- and Patlak analysis-based methods for determining vascular permeability

Joe Tien<sup>a,b,\*</sup>, Xuanyue Li<sup>a</sup>, Raleigh M. Linville<sup>a</sup>, Evan J. Feldman<sup>a</sup>

<sup>a</sup> Department of Biomedical Engineering, Boston University, 44 Cummington Mall, Boston, MA 02215, USA

<sup>b</sup> Division of Materials Science and Engineering, Boston University, 15 St. Mary's Street, Brookline, MA 02446, USA

## ARTICLE INFO

### Keywords:

Patlak equation  
Compartmental model  
Magnetic resonance imaging  
Computed tomography  
Microcirculation

## ABSTRACT

This study describes a computational algorithm to determine vascular permeability constants from time-lapse imaging data without concurrent knowledge of the arterial input function. The algorithm is based on “blind” deconvolution of imaging data, which were generated with analytical and finite-element models of bidirectional solute transport between a capillary and its surrounding tissue. Compared to the commonly used Patlak analysis, the blind algorithm is substantially more accurate in the presence of solute delay and dispersion. We also compared the performance of the blind algorithm with that of a simpler one that assumed unidirectional transport from capillary to tissue [as described in Truslow et al., *Microvasc. Res.* 90, 117–120 (2013)]. The algorithm based on bidirectional transport was more accurate than the one based on unidirectional transport for more permeable vessels and smaller extravascular distribution volumes, and less accurate for less permeable vessels and larger extravascular distribution volumes. Our results indicate that blind deconvolution is superior to Patlak analysis for permeability mapping under clinically relevant conditions, and can thus potentially improve the detection of tissue regions with a compromised vascular barrier.

## 1. Introduction

Quantitative measurement of vascular permeability is a cornerstone of microvascular physiology, both for basic studies of the microcirculation and for clinical assessment of conditions that involve breakdown of the vascular barrier. These measurements have relied almost exclusively on injecting a labeled solute or contrast agent into a blood vessel that feeds the tissue to be analyzed, and then fitting time-lapse imaging data to a two-compartment model of solute uptake (Fig. 1A) (Patlak et al., 1983):

$$\frac{dI}{dt} = \frac{dI}{dt} + \alpha_0 I_v \quad (1)$$

Here,  $I(t)$  is the spatially integrated signal in the tissue region-of-interest (ROI), which includes signals from vessels within the tissue;  $I_v(t)$  is the spatially integrated signal that originates from the vessels within the ROI; and  $\alpha_0$  is the permeability product  $PS/V_p$ , where  $P$  is the solute permeability coefficient,  $S$  is the vascular surface area, and  $V_p$  is the intravascular distribution volume for the solute in the ROI. The

parameter  $\alpha_0$  is analogous to a rate constant and has units of 1/time. It is assumed that the imaging data are suitably transformed so that they are proportional to solute concentrations.

Although measurement of the tissue signal  $I$  is routinely performed, intravascular solute cannot be distinguished from extravascular solute at the level of microvessels with current clinical imaging techniques, which have typical spatial resolutions of  $\geq 0.5$  mm (Lin and Alessio, 2009). Thus,  $I_v$  is generally unknown, and Eq. (1) cannot be solved for the permeability  $\alpha_0$ . In the experimental setting, this problem can be avoided by rapid and sustained microinjection of labeled solute at a defined time immediately upstream of the ROI (Huxley et al., 1987). In the clinical setting, however, solute injection takes place at an artery that is distant from the ROI (Calamante et al., 2000; Meyer, 1989). As a result, clinical permeability imaging requires the separate measurement of an arterial input function  $AIF(t)$ , i.e., the solute signal from a proximal artery, which is assumed to equal  $I_v(t)/V_p$ . With this assumption, the transport equation becomes:

**Abbreviations:** AIF, arterial input function; ATH, adiabatic tissue homogeneity; CT, computed tomography; MRI, magnetic resonance imaging; PET, positron emission tomography; ROI, region-of-interest; SNR, signal-to-noise ratio; 2CXM, two-compartment exchange model.

\* Corresponding author at: Department of Biomedical Engineering, Boston University, 44 Cummington Mall, Boston, MA 02215, USA.

E-mail address: [jtien@bu.edu](mailto:jtien@bu.edu) (J. Tien).

<https://doi.org/10.1016/j.mvr.2020.104102>

Received 25 February 2020; Received in revised form 1 September 2020; Accepted 4 November 2020

Available online 6 November 2020

0026-2862/© 2020 Elsevier Inc. All rights reserved.

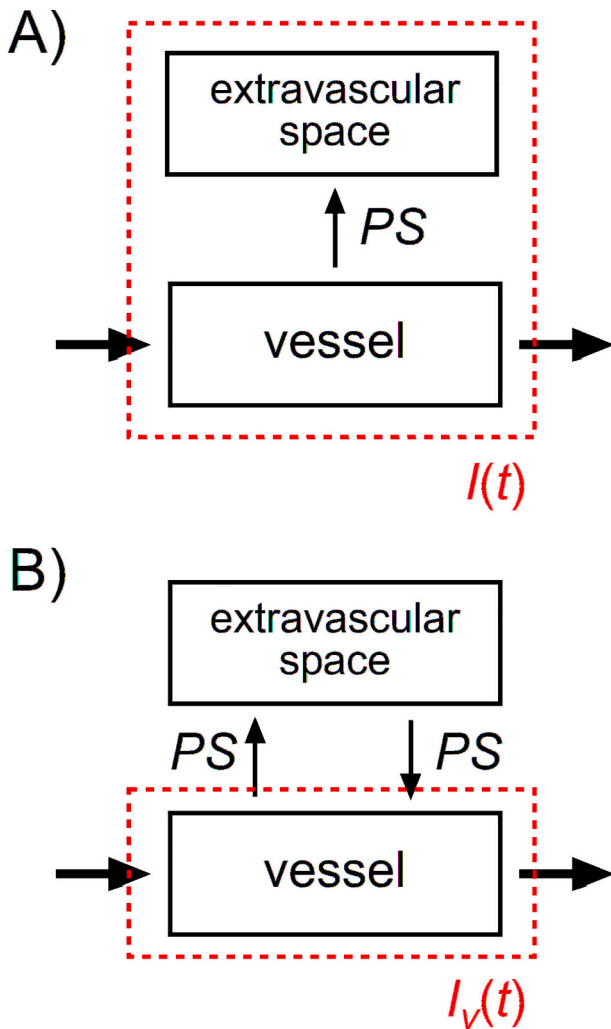


**Fig. 1.** Block diagrams of the transport models used in this study. (A) Unidirectional model that neglects return of solute from the tissue to the vascular space. This model was used in the blind algorithm developed in a previous study (Truslow and Tien, 2013). (B) Bidirectional model that allows for solute uptake and return. In both cases, the vascular and tissue compartments are assumed to be separately well-mixed.  $PS$  represents the solute clearance across the vessel wall. Vascular flow (denoted by thick arrows) is assumed to be much larger than  $PS$ . Dotted lines denote the regions that are used to obtain the spatially integrated intensities  $I$  and  $I_v$ ; for clarity, only one integration region is shown per diagram.

$$\frac{dI}{dt} = V_p \frac{d(AIF)}{dt} + \alpha_0 V_p AIF \quad (2)$$

Standard Patlak analysis estimates the permeability constant  $\alpha_0$  (and the vascular volume  $V_p$ ) at each image pixel by integrating Eq. (2) over time and using a linear fit of  $I(t)/AIF(t)$  versus  $\int_0^t AIF(t)dt/AIF(t)$  (Peters, 1994). This approach assumes that the intravascular solute transit time is negligible, and that only uptake of solute is possible. Its mathematical simplicity has made Patlak analysis one of the most widely applied methods for clinical assessment of vascular permeability, including in perfusion CT for management of ischemic stroke and whole-body PET for detection of tumors (Hom et al., 2011; Karakatsanis et al., 2013). Modified plots that take solute return into account have been developed, but they are more sensitive to noise and are not considered here (Karakatsanis et al., 2015; Logan et al., 1990; Patlak and Blasberg, 1985).

It is important to recognize that the AIF is not exactly proportional to the intravascular signal  $I_v$ . Typical transit times from the site at which AIF is measured to the ROI are on the order of seconds. As a result,  $I_v$  is a

time-delayed and broadened version of the AIF. If not corrected for, solute delay and dispersion can lead to large errors in estimated permeabilities when a standard Patlak analysis is applied (Schneider et al., 2011). Other sources of error, such as partial volume effects, further limit the ability of the AIF to represent  $I_v$  accurately (Chen et al., 2004). Several studies have attempted to correct for these phenomena, largely by assuming particular expressions for intravascular solute transport between the site of AIF measurement and the ROI (Dankbaar et al., 2008a; Dankbaar et al., 2008b; Hom et al., 2009; Schneider et al., 2011).

To obtain permeability values without knowledge of the vascular input, we and others have attempted “blind” deconvolution of solute imaging data (Fluckiger et al., 2009; Grüner and Tact, 2006; Riabkov and Di Bella, 2002; Schabel et al., 2010; Tact et al., 2012; Truslow and Tien, 2013). Most blind approaches are “multichannel” ones, i.e., they compare imaging data from two or more ROIs to deduce the AIF, which is assumed to be the same among all ROIs (Feng et al., 1997; Riabkov and Di Bella, 2002; Yang et al., 2004; Yankeelov et al., 2005). “Single-channel” methods, which rely on imaging data from a single ROI, take advantage of known properties of a desired signal (e.g., non-negativity) and choose the most likely signal that displays these properties (Tact et al., 2012; Tact et al., 2015; Truslow and Tien, 2013). By not requiring an AIF, these blind deconvolution methods can potentially avoid errors associated with solute delay and dispersion, and thus may improve the accuracy of image-guided treatment.

It is important to recognize that whether imaging data are processed with blind deconvolution or with methods that require an AIF, the model of vascular permeability described by Eq. (1) makes several assumptions. First, the extravascular concentration of solute is taken to be much smaller than the intravascular concentration. Second, the intra- and extravascular compartments are assumed to be separately well-mixed. Third, the solute transport is treated as unidirectional from vessel to tissue; reabsorption of solute into the bloodstream is not considered. In general, these assumptions hold for short times after vascular injection of solute and for vessels that do not have a compromised barrier. They are less valid during imaging of tissues that contain highly permeable vessels, such as those that arise during injury, inflammation, or cancer.

The objectives of the present study are thus two-fold. First, this study extends our previous blind deconvolution algorithm to a bidirectional model of vascular permeability that allows for tissue-to-vessel transport. Second, it compares the ability of the three different algorithms—those based on Patlak analysis (Peters, 1994), the previous blind approach using the unidirectional transport model (Truslow and Tien, 2013), and the new blind approach using the bidirectional transport model—to correctly predict vascular permeability. Our data demonstrate that both implementations of blind deconvolution are more accurate than Patlak analysis is when the AIF is delayed and dispersed, as would be the case in clinical imaging. Analysis of imaging data with the bidirectional transport model was more accurate than with the simpler unidirectional one for the combination of high vascular permeability and high vascular volume.

## 2. Numerical methods

### 2.1. Bidirectional compartmental model of solute transport

The bidirectional transport model [also known as the “extended Tofts” model (Sourbron and Buckley, 2013)] includes the possibility of solute backflow (Fig. 1B):

$$\frac{dI}{dt} = \frac{dI_v}{dt} + \alpha_0 I_v - k_0 (I - I_v) \quad (3)$$

The last term in Eq. (3) accounts for reabsorption of solute into the vessel lumen, with a rate constant  $k_0$ . Here,  $k_0$  equals  $PS/V_e$ , where  $V_e$  is the extravascular distribution volume for the solute in the ROI, and  $P$  and  $S$  are as defined earlier; as the rate constant for solute return, it has

units of 1/time. The permeability products  $\alpha_0$  and  $k_0$  are related by the ratio of solute distribution volumes:

$$k_0 = \frac{V_p}{V_e} \alpha_0 \quad (4)$$

Eq. (3) can be solved to give:

$$I_v(t) = I(t) - \alpha_0 e^{-(\alpha_0+k_0)t} \int_0^t e^{(\alpha_0+k_0)t} I(t) dt \quad (5)$$

We assume that the vascular solute concentration is initially zero at time  $t = 0$ , rises to a maximum, then decreases smoothly back to zero at time  $t = T$ . That is,  $T$  refers to the time period between the first and last time-points used in the algorithm; if all imaging data are to be considered, as in the current study, then  $T$  also equals the end of the imaging time.

For a given or measured intensity function  $I(t)$  and guesses of  $\alpha$  and  $k$ , we can calculate a predicted vascular signal:

$$\tilde{I}_v(t; \alpha, k) = I(t) - \alpha e^{-(\alpha+k)t} \int_0^t e^{(\alpha+k)t} I(t) dt \quad (6)$$

Our method of determining permeability constants consists of searching for the values of  $\alpha$  and  $k$  that yield a vascular signal  $\tilde{I}_v(t; \alpha, k)$  that simultaneously displays a value and slope of zero at the end of the time series. As shown in the Appendix, this search—assuming it converges—will yield the correct  $\alpha_0$  and  $k_0$ . Because  $I(t)$  is measured clinically only at a finite set of times  $t_i, i = 1, \dots, N$ , Eq. (6) must be discretized first:

$$\tilde{I}_v(t_i; \alpha, k) = I(t_i) - \alpha e^{-(\alpha+k)t_i} \sum_{j=1}^N [c_j e^{(\alpha+k)t_j} I(t_j)] \quad (7)$$

where the  $c_j$  are coefficients chosen to implement an extended form of Simpson's Rule (Yang et al., 2004). The search algorithm starts at  $\alpha = k = 0$ , which leads to  $\tilde{I}_v(t_i) = I(t_i)$ . We first increase  $\alpha$  until the predicted long-term vascular signal  $\tilde{I}_v(T)$  is zero. We then increase  $k$  by a small increment, and repeat the procedure to map the values of  $\alpha$  and  $k$  where  $\tilde{I}_v(T; \alpha, k) = 0$ . In principle, this “staircase” search strategy should eventually yield the values of  $\alpha$  and  $k$  where  $\tilde{I}_v(T; \alpha, k)$  and  $d\tilde{I}_v(T; \alpha, k)/dt$  are simultaneously zero; these values represent the best estimates of the permeability products  $\alpha_0$  and  $k_0$ .

## 2.2. Application to solute intensity data from analytical two-compartment models

To optimize the blind algorithm for prediction of vascular permeabilities, we first selected a vascular signal  $I_v(t)$  that contained a single bolus or additional terms to represent solute recirculation and a slowly decaying residual signal [Eqs. (11) and (12) in the Appendix]. We then solved Eq. (3) to obtain the theoretical  $I(t)$  for the particular  $I_v$  and true permeability values  $\alpha_0$  and  $k_0$ . Discrete sampling of  $I(t)$  provided an intensity signal that served as the input dataset for the algorithm. Gaussian noise with a signal-to-noise ratio (SNR) of at least 20 was added to  $I$ , and the blind algorithm was executed to yield the predicted permeability values  $\alpha$  and  $k$ ; this process was performed for at least three hundred noisy simulations. We chose Gaussian noise for computational convenience, although other types of noise that are specific to a particular imaging modality (e.g., Poisson in PET imaging) could be applied instead (Gravel et al., 2004). The long-term value and slope of the predicted vascular signal  $\tilde{I}_v(t; \alpha, k)$  were calculated from an averaging window that extended from  $t = T-\Delta T$  to  $t = T$ . Median, 5th percentile, and 95th percentile values of  $\alpha$  and  $k$  were obtained for each model. We also noted the frequency at which the algorithm did not converge or at which it incorrectly predicted  $k$  to equal zero.

## 2.3. Application to solute intensity data from finite-element models of capillary and tissue transport

We then applied the optimized blind algorithm to solute intensity profiles that were obtained from finite-element models of solute transport in a capillary-containing tissue cylinder, effectively performing an “in silico” imaging experiment. The diameters of the capillary and tissue cylinder were 5  $\mu\text{m}$  and 15–45  $\mu\text{m}$ , respectively, and the lengths of the capillary and tissue cylinder were both 1 mm; the capillary and tissue were co-axial. The finite-element models accounted for the convection of solute (intravascular and extravascular diffusion coefficients of 250 and 100  $\mu\text{m}^2/\text{s}$ , respectively; maximum capillary flow speed of 600  $\mu\text{m}/\text{s}$ ). The input to the capillary included terms to simulate solute recirculation and residual vascular signal, and was time-shifted to represent a delay of 5 or 10 s [Eq. (13) in the Appendix]. The solute concentration was spatially integrated over the entire volume (including the capillary space) to yield  $I(t)$  at discrete times up to  $t = 75$  or 80 s for delays of 5 or 10 s, respectively. Gaussian noise was then added to  $I$ , and the resulting intensity signal was used as the input to the permeability algorithm. For each finite-element model, at least three hundred noisy simulations were performed. All finite-element models were solved with COMSOL Multiphysics ver. 5.4 (Comsol, Inc.), and models were meshed iteratively until two sequential meshes yielded  $I(t)$  curves that differed by <0.5% before noise was added.

For comparison, blind analysis was performed on the same data, but with the permeability value  $k$  artificially constrained to zero; this analysis replicated the previous blind algorithm based on unidirectional solute transport (Truslow and Tien, 2013). Patlak analysis was also performed on the same intensity data (Peters, 1994). Here, the arterial input function  $AIF(t)$  was assumed to be a less-dispersed form of  $I_v$  and was shifted earlier in time relative to  $I_v$  [Eq. (14) in the Appendix]. A linear fit of  $I(t)/AIF(t)$  versus  $\int_0^t AIF(t) dt/AIF(t)$  yielded  $\alpha$ . Because Patlak analysis is based on a unidirectional solute transport model, it also assumes  $k$  is zero.

## 3. Results

### 3.1. Application of blind permeability algorithm to noise-free data

Fig. 2 illustrates the basic ideas that underlie the permeability algorithm, for a simple bolus vascular signal  $I_v(t)$  of finite width with true permeability constants  $\alpha_0 = 0.05/\text{s}$  and  $k_0 = 0.0025/\text{s}$ . The bolus was modeled without delay or recirculation (Fig. 2A). This vascular signal resulted in a tissue intensity  $I(t)$  that rose simultaneously with  $I_v$ , but did not decrease back to zero by the end of the sampling period (Fig. 2B). Sampling  $I(t)$  once per second over a total time of  $T = 60$  s yielded a noise-free time series (Fig. 2C) that we used to test the accuracy of the algorithm without the confounding effects of noise. Using Eq. (7) with  $\alpha = \alpha_0$  and  $k = k_0$  yielded a predicted vascular signal  $\tilde{I}_v(t; \alpha, k)$  that nearly matched the theoretical  $I_v$  (Fig. 2D, center). Deviating from these ideal values led to characteristic changes in the shape of the predicted  $\tilde{I}_v$ . An iterative search with a resolution of  $5 \times 10^{-5}/\text{s}$  yielded  $\alpha = 0.05/\text{s}$  and  $k = 0.0025/\text{s}$  as the values for which the long-term vascular signal and slope were exactly zero; thus, the error that resulted from discretization at the sampling frequency of 1 Hz was negligible for this case.

### 3.2. Optimization of the blind permeability algorithm in presence of noise

To determine the optimal imaging conditions that yield the most accurate permeability predictions in the presence of noise, we varied the time period  $T$  between the first and last time-points used in the algorithm, the size of the averaging time window  $\Delta T$ , and the signal-to-noise ratio SNR. These simulations were performed with the same bolus vascular signal and theoretical permeability values described above. In preliminary work, we found that more frequent time sampling always

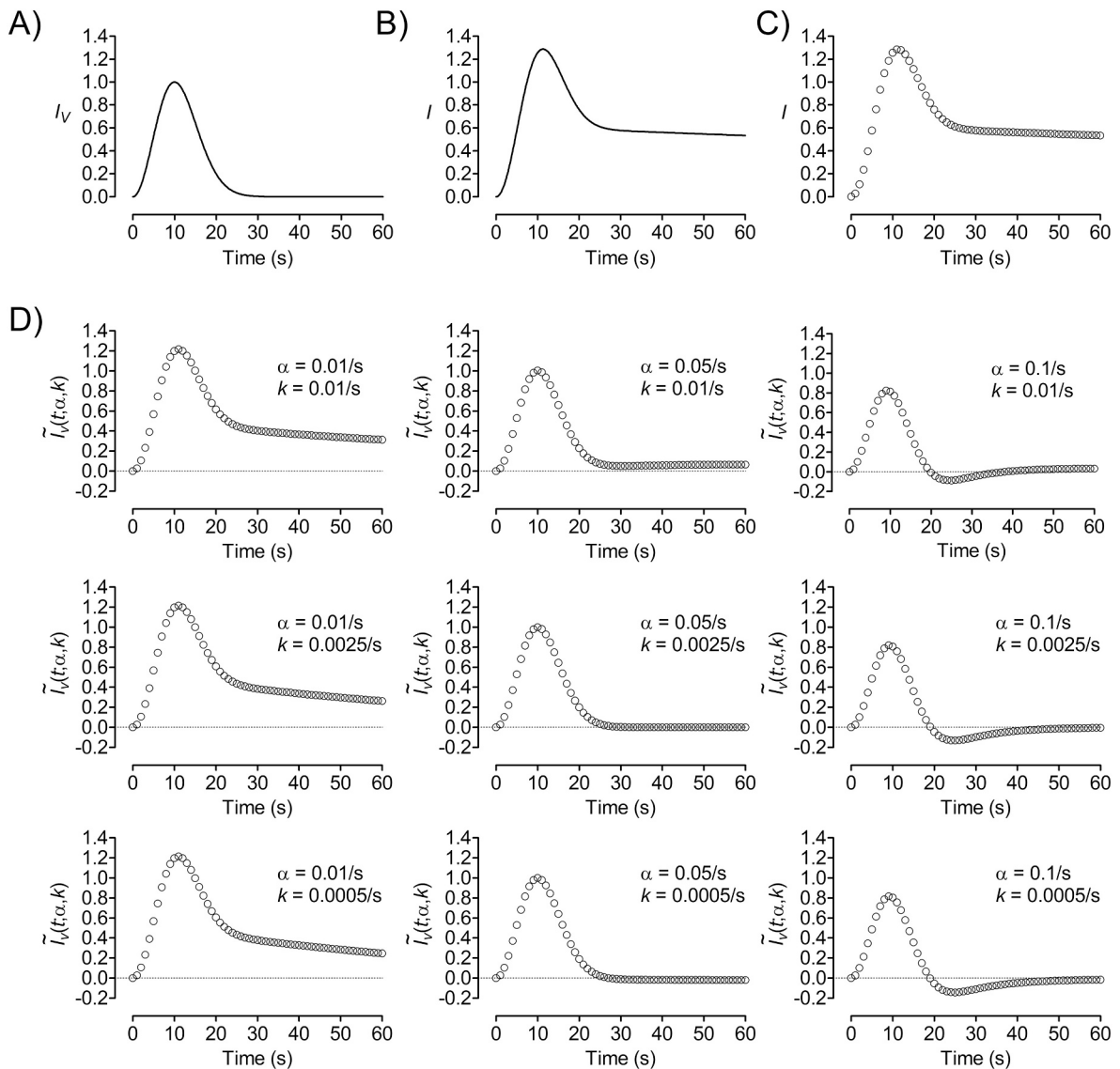


**Fig. 2.** Representative example of the permeability algorithm. (A) Vascular signal  $I_v(t)$  for a bolus injection, generated from Eq. (11) in the Appendix with  $\tau = 10$  s. (B) Corresponding tissue signal  $I(t)$  for true permeability constants  $\alpha_0 = 0.05/s$  and  $k_0 = 0.0025/s$ , found from solving Eq. (3). (C) Discretely sampled  $I(t)$  with a sampling frequency of 1 Hz. (D) Predicted vascular signal  $\tilde{I}_v(t; \alpha, k)$ , for various values of  $\alpha$  and  $k$ . The predicted  $\tilde{I}_v$  has a long-term value and slope of zero when  $\alpha = 0.05/s$  and  $k = 0.0025/s$ . Calculation of the long-term value and slope used the last two time-points (i.e.,  $\Delta T = 1$  s).

led to more accurate permeabilities; thus, we selected the highest sampling frequency (1 Hz) that was consistent with typical clinical imaging. For the other parameters, we first varied  $T$ , then  $\Delta T$ , and finally  $SNR$  to determine the main factors that control the accuracy of the permeability algorithm for this particular vascular signal.

Varying the time  $T$  revealed that at least 35–40 s were needed to avoid large permeability overestimates (Fig. 3A). Surprisingly, for noisy imaging data with  $SNR = 40$ , the algorithm often did not converge or yielded  $k = 0$  when the time period was greater than 45–50 s. This result suggests that the increased variability when predicting permeabilities from long, noisy imaging data originated from the effects of noise on the determination of the long-term value and slope of the vascular signal.

One potential strategy for mitigating the effects of noise is to change the length of the averaging time window that is used to obtain the long-term vascular signal and slope. As expected, short time windows led to large errors in predicted permeabilities and greater chances of algorithm errors (Fig. 3B). In contrast, long averaging windows eliminated algorithm errors, but a systematic overestimation of both  $\alpha$  and  $k$  emerged.

Finally, we determined how the accuracy of the algorithm depended

on signal-to-noise ratio  $SNR$  (Fig. 3C). As expected, higher  $SNR$  led to more accurate predictions. At a clinically achievable value of  $SNR = 40$ , the blind algorithm predicted  $\alpha$  to within 12%.

### 3.3. Accuracy of the optimized blind permeability algorithm

The above results suggest that the blind algorithm performs best with long imaging times and averaging windows of roughly half the time period. We selected optimized imaging conditions of  $T = 60$  s and averaging window of thirty time-points (i.e.,  $\Delta T = 29$  s); the imaging frequency and signal-to-noise ratio were kept at 1 Hz and 40, respectively. These choices are consistent with current clinical imaging practice in perfusion CT (Dankbaar et al., 2008b); application of the algorithm to the longer (several minutes) time periods that are more common in perfusion MRI is considered in the Discussion. With these conditions, we performed a parametric sweep to determine the accuracy of the permeability algorithm across a wide range of true permeability values  $\alpha_0$  (Fig. 4A) and  $k_0$  (Fig. 4B). In general, the errors in  $\alpha$  tended to be substantially smaller than those in  $k$ . Across the ranges of values

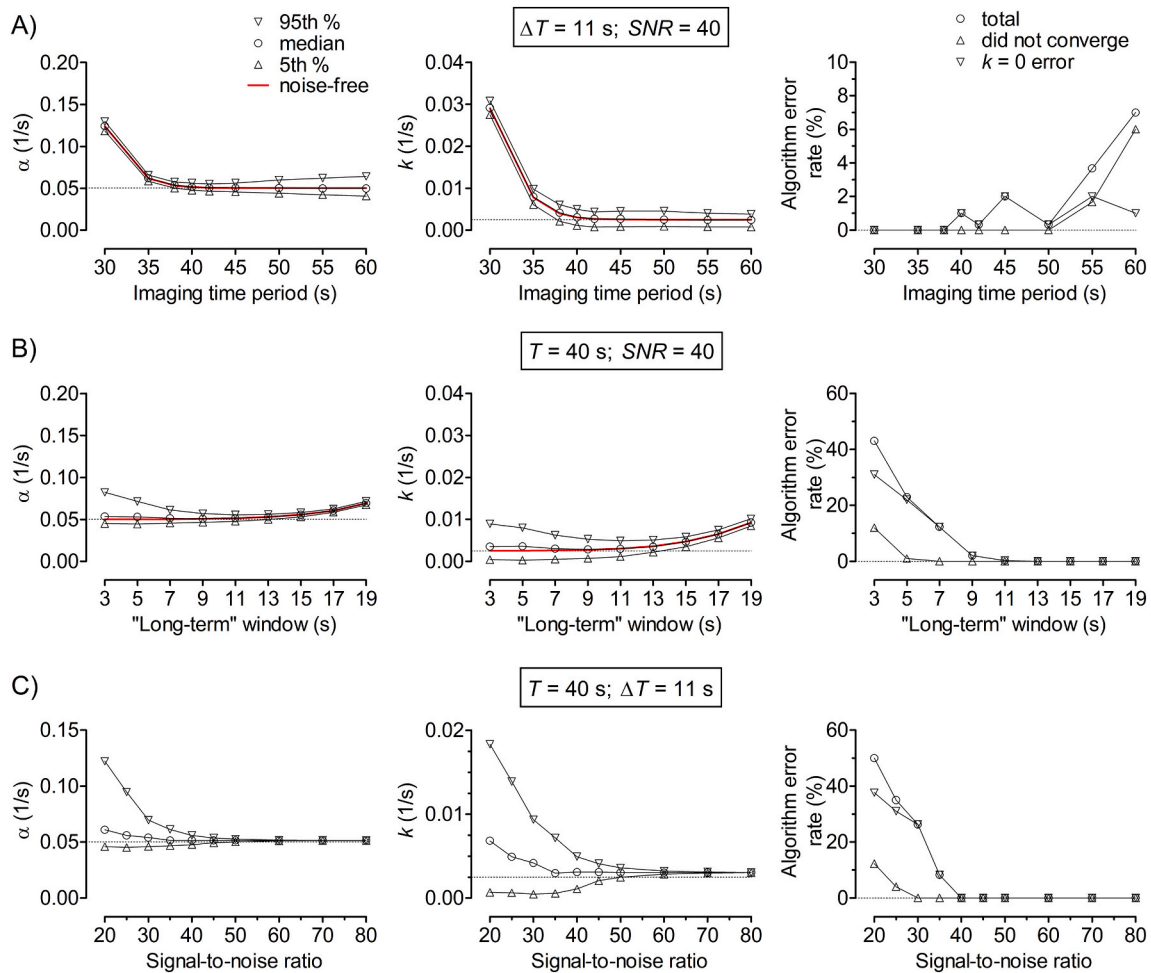


**Fig. 3.** Predicted permeability constants  $\alpha$  and  $k$  and frequency of algorithm error, as functions of (A) imaging time period  $T$ , (B) length of averaging time window  $\Delta T$ , and (C) signal-to-noise ratio  $SNR$ . The “base case” model for these simulations had  $\alpha_0 = 0.05/s$ ,  $k_0 = 0.0025/s$ ,  $T = 40$  s,  $\Delta T = 11$  s, and  $SNR = 40$ . The vascular input  $I_v$  was identical to the one used in Fig. 2.

examined,  $\alpha$  was predicted to within  $\sim 10\%$  error, while the error in  $k$  depended on the true permeability values. For small  $\alpha_0$  or  $k_0$ , the algorithm predicted  $k$  poorly, with errors on the order of 100% for the smallest  $\alpha_0$  and  $k_0$  examined.

We also determined the accuracy of the algorithm when the vascular signal did not decay to zero by the end of the imaging time (Fig. 4C). These simulations were intended to model the presence of solute recirculation, which is often present with clinical imaging protocols. Residual vascular signal (i.e., the ratio of the vascular intensity at the last time-point to the peak vascular intensity) of  $\sim 2\%$  resulted in a 20–40% overestimate in  $\alpha$  for a true  $\alpha_0$  of 0.05/s.

### 3.4. Application to spatially and temporally resolved solute transport data

The above analysis treats microvascular solute transport with a two-compartment model, which assumes that the compartments (i.e., the intra- and extravascular spaces) are separately well-mixed. When the vascular flow speed is limiting and/or when the inter-vessel spacing is large, solute concentration gradients may be substantial. Thus, we performed a more stringent test of the blind algorithm by using computed imaging data that were extracted from finite-element models of solute transport. These models did not assume the existence of well-mixed compartments and served as “in silico” imaging experiments.

In these simulations, we modeled the transport of solute within a capillary-containing tissue cylinder. The vascular input to the capillary consisted of a delayed and dispersed signal that decayed to a residual of

$\sim 1\%$  [Eq. (13) in the Appendix]. The solute concentration within the tissue cylinder, including that in the capillary space, was spatially integrated to yield the amount of solute as a function of time. This volume-integrated signal was analogous to an intensity signal in a single pixel from clinical imaging, and was used as the input to the permeability algorithm.

Following the optimized parameters, we set the total time period to be 75 or 80 s (with sampling frequency 1 Hz) and used the last thirty time-points as the averaging window; we also applied a signal-to-noise ratio of 40. We varied the solute permeability coefficient  $P$ , the tissue cylinder radius  $r_t$ , and the solute input delay times. The true permeability constants were calculated as  $\alpha_0 = 2P/r_0$  and  $k_0 = 2Pr_0/(r_t^2 - r_0^2)$ , where  $r_0 = 2.5 \mu\text{m}$  is the capillary radius. For comparison, we analyzed the same simulated data with a blind algorithm based on unidirectional transport (Truslow and Tien, 2013) and with Patlak analysis (Peters, 1994), both of which assume fast vascular mixing but neglect extravascular accumulation of solute.

These analyses showed that the new and previous blind algorithms predicted the permeability constant  $\alpha_0$  more accurately than Patlak analysis did, across a broad range of permeabilities and intercapillary spacings (Fig. 5A). The blind algorithm with a bidirectional transport model consistently overestimated  $\alpha_0$  by 40–70%, with larger errors for smaller  $\alpha_0$ . The blind algorithm with a unidirectional transport model overestimated  $\alpha_0$  by 10–20% in most cases, except for the combination of small intercapillary spacings (15 or 25  $\mu\text{m}$ ) and large permeabilities ( $\alpha_0$  of 0.05 or 0.1/s) where  $\alpha_0$  was underestimated by up to  $\sim 2$ -fold. The

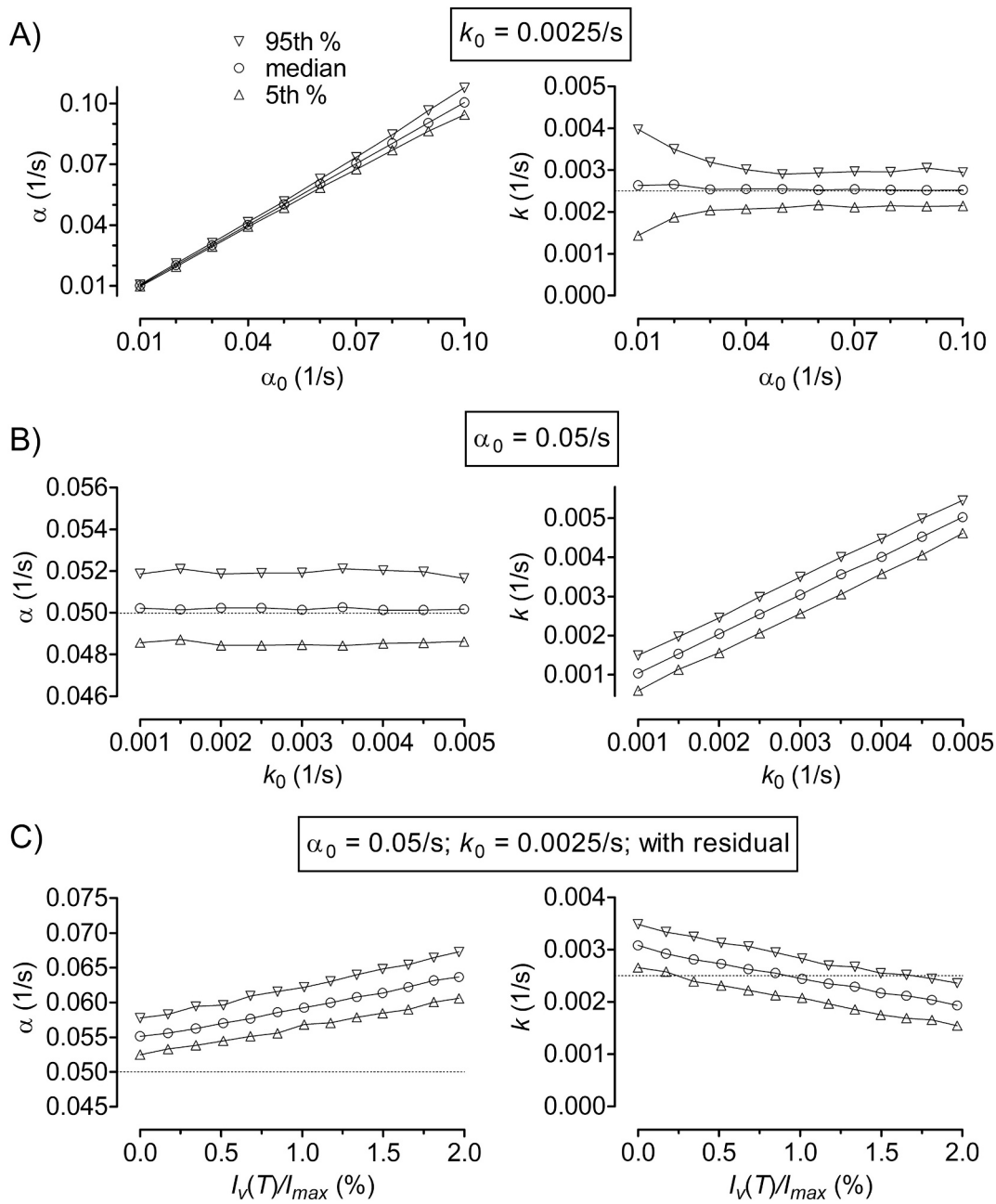


**Fig. 4.** Predicted permeability constants  $\alpha$  and  $k$ , as functions of true permeability values (A)  $\alpha_0$  and (B)  $k_0$ , and (C) the residual vascular signal.  $I_{max}$  refers to the maximum value of  $I_v(t)$  over the imaging period; its ratio with  $I_v(T)$  represents the residual vascular signal at the last time-point. The “base case” model for these simulations had  $\alpha_0 = 0.05/s$ ,  $k_0 = 0.0025/s$ ,  $T = 60$  s,  $\Delta T = 29$  s, and  $SNR = 40$ ; for (C),  $T = 70$  s. The vascular inputs for (A) and (B) were identical to that used in Figs. 2 and 3; the input for (C) was generated from Eq. (12) of the Appendix.

bidirectional transport model yielded more accurate estimates of  $\alpha_0$  for these latter cases. The accuracy of Patlak analysis was noticeably worse than that for either blind algorithm in all cases, and worst for small intercapillary spacings.

The predicted values of  $k$  from a bidirectional transport model were accurate only for small intercapillary spacings (15 or 25  $\mu m$ ) and large permeabilities ( $\alpha_0$  of 0.05 or 0.1/s) (Fig. 5B). Large intercapillary spacing and/or small permeabilities result in extremely small values of  $k_0$  that could not be reliably predicted. By definition, the unidirectional transport model and Patlak analysis (which assumes solute uptake only) do not yield values for  $k$ .

To aid in visualization, we used the algorithm to “map” the permeability in a rectangular array, in which each element of the array represents one simulation of a specific combination of permeability

constant and capillary spacing (Figs. S1, S2). These images provide a different way to visualize the predictions, in a format more akin to a permeability map. They show that the bidirectional and unidirectional blind algorithms yield permeabilities that are less scattered and approach the theoretical values more closely than the predictions of Patlak analysis do.

#### 4. Discussion

The algorithm that this study developed successfully predicted vascular permeability without knowledge of an arterial input function (AIF). These values consisted of the permeability-surface area product normalized to the vascular or extravascular volumes (i.e.,  $\alpha_0 \equiv PS/V_p$  and  $k_0 \equiv PS/V_e$ ). Although the AIF can be measured in clinical imaging

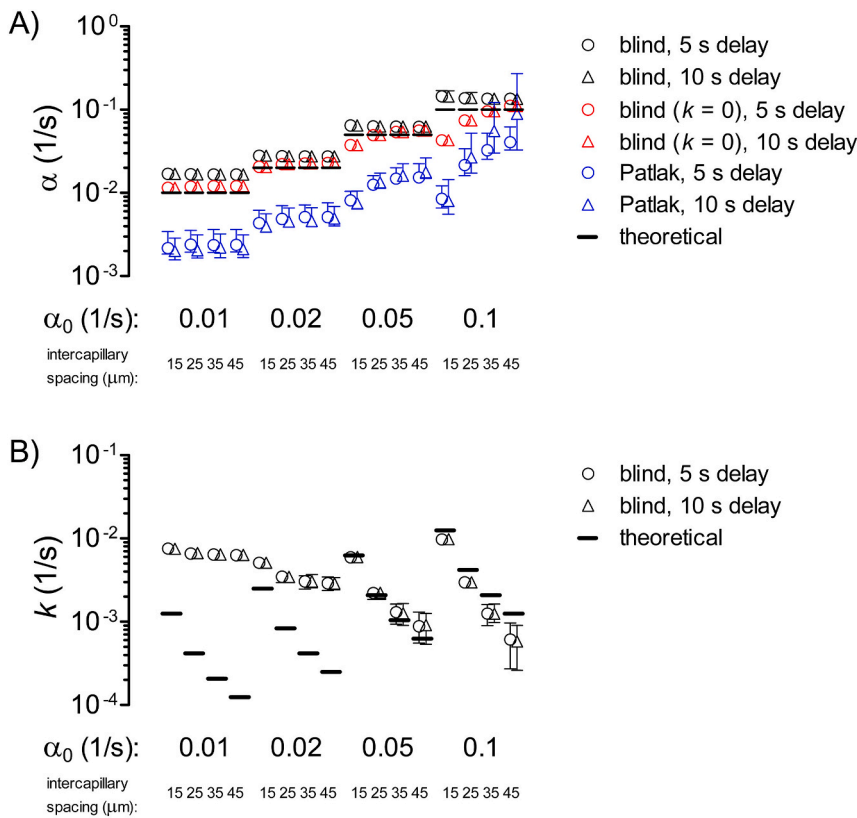


**Fig. 5.** Predicted permeability constants  $\alpha$  and  $k$ , using imaging data that were generated from finite-element models of solute transport in a capillary-containing tissue cylinder. (A) Theoretical  $\alpha_0$  (black lines) and predicted  $\alpha$  (open symbols) from blind deconvolution with the bidirectional and unidirectional ( $k = 0$ ) transport models and from Patlak analysis. (B) Theoretical  $k_0$  (black lines) and predicted  $k$  (open symbols) from blind deconvolution with the bidirectional model. Median, 5th percentile, and 95th percentile values are plotted; in some cases, the confidence intervals are smaller than the symbols and are not visible. The vascular input was a delayed version of the one used in Fig. 4C, and was generated by Eq. (13) in the Appendix. For Patlak analysis, the AIF was generated by Eq. (14) in the Appendix.

by selectively analyzing the signal intensity within a feeding artery, the actual vascular input to a given tissue voxel is delayed and dispersed relative to the AIF and can be subject to partial volume effects in small arteries (Chen et al., 2004). By not requiring the measurement of an AIF, our blind algorithm is inherently robust against errors associated with vascular delay and dispersion.

At first, it may seem implausible that enough information could be obtained solely from time-lapse imaging data  $I(t)$  to obtain permeability values. After all,  $I(t)$  is a convolution of an unknown vascular input and unknown vascular permeabilities  $\alpha_0$  and  $k_0$ . Nevertheless, blind deconvolution has been performed successfully in other fields, by relying on prior knowledge of certain qualities of the unknown signal (Fish et al., 1995). In the current study, these requirements consisted of: 1)  $I_v(t)$  decays to zero by the end of the imaging time, 2)  $I_v(t)$  reaches a slope of zero by the end of the imaging time, and 3)  $I_v(t)$  is non-negative. In practice, enforcing the first two conditions was sufficient to obtain unique predicted permeability constants  $\alpha$  and  $k$ .

#### 4.1. Comparison of blind and Patlak analyses of vascular permeability

Compared with Patlak analysis, the blind algorithm described here performed very well. Because it does not rely on an AIF, it is inherently unaffected by solute delay and dispersion. In contrast, Patlak analysis often yields erroneous values when the solute is delayed, and subjective interpretation of the resulting plots may be needed. The clinical implication is that permeability predictions that are based on Patlak analysis will be prone to false negatives and/or false positives, and regions of abnormal vascular permeability will have less distinct boundaries, compared to those generated by blind deconvolution. These limitations become especially noticeable when our results are represented as color maps (Fig. S1).

Our results also show that any advantage of choosing a bidirectional over a unidirectional transport model to analyze solute imaging data depends on the true permeability and vascular spacing. In principle, a

model that allows for the return of solute from tissue to capillary should be more physiological than one that only allows for solute uptake. Nevertheless, we found that unidirectional models yielded more accurate values of  $\alpha$  than bidirectional models did, for most cases examined (Fig. 5A). The exceptions were when  $\alpha_0$  was  $\geq 0.05/\text{s}$  and the capillary spacing was  $\leq 25 \mu\text{m}$  (equivalent to  $PS$  of  $\geq 12 \text{ mL}/100 \text{ mL}/\text{min}$  and  $V_p$  of  $\geq 4 \text{ mL}/100 \text{ mL}$ ), for which the bidirectional models were more accurate. The bidirectional model yields an additional permeability measure  $k$  that can be used to infer the tissue solute distribution volume, but we have found that the predicted values of  $k$  are only accurate for large permeabilities.

These results can be rationalized by considering the relevant solute mean transit times. The intravascular transit time is  $V_p/F_p$ , where  $F_p$  is the capillary flow rate; in our finite-element models, this time is 3.3 s. The extravascular transit time is  $V_e/PS$ , which ranges from 80 s (for the combination  $\alpha_0 = 0.1/\text{s}$  and  $15 \mu\text{m}$  spacing) to 8000 s (for the combination of  $\alpha_0 = 0.01/\text{s}$  and  $45 \mu\text{m}$  spacing). Since we held the imaging time period to  $\leq 80$  s, only for large permeabilities and small vascular spacings would one expect solute return from the extravascular space to contribute noticeably to transport rates. As a result, for small permeabilities and/or large spacings, the bidirectional model is effectively underdetermined or over-parameterized, and the predictions of the blind algorithm would be less accurate than for the unidirectional model.

One might expect that Patlak analysis would also outperform the bidirectional model for small permeabilities and/or large spacings, since solute return is negligible for these cases. Our results show that Patlak analysis was still less accurate than the blind algorithms, even for these cases. The reason for this finding is that solute delay and dispersion make the measured AIF different from the true vascular input. Indeed, when we used the delayed and dispersed vascular input [Eq. (13)] as the AIF instead of Eq. (14), Patlak analysis yielded essentially perfect permeability predictions (data not shown). We note that corrections for solute delay and dispersion have been developed (Schneider et al., 2011;

Willats et al., 2006), albeit at the cost of greater computational complexity. The practical advantage of the blind algorithms over Patlak analysis will depend on the degree to which these corrections can compensate for delay and dispersion.

#### 4.2. Comparison with other models of vascular permeability and other blind deconvolution approaches

The blind algorithms described in this study and in a previous one (Truslow and Tien, 2013) are based on the two-compartment bidirectional (extended Tofts) and unidirectional models of solute transport, which assume that the intravascular solute transit time is negligible and that the vascular and extravascular compartments are separately well-mixed. Other transport models, with their own sets of assumptions, have been used in previous studies (Koh et al., 2011; Sourbron and Buckley, 2011; Sourbron and Buckley, 2012). The standard Tofts model neglects the vascular space (i.e., it sets  $V_p \approx 0$ ) and is well-suited for weakly vascularized tissues, such as the normal brain (Sourbron and Buckley, 2011). The two-compartment exchange model (2CXM) does not assume negligible intravascular transit time, and includes vascular flow as a separate parameter (Brix et al., 1999). The adiabatic tissue homogeneity (ATH) model further assumes that only the extravascular compartment is well-mixed (St. Lawrence and Lee, 1998). Distributed models that do not assume mixing of the extravascular compartment exist as well (Goresky et al., 1970).

Whether the models that are used in the current study are sufficient to describe a given tissue depends on the flows, vascular volumes, and permeabilities of that tissue. Previous studies that fit identical imaging data to different models have shown that, for the best accuracy, the model should be matched to the imaging data (Cramer and Larsson, 2014; Cuenod and Balvay, 2013; Oosterbroek et al., 2015; Sourbron and Buckley, 2011). Use of a complex model with too many fitting parameters for the given data can often lead to less physiological values of these parameters (Sourbron and Buckley, 2011). For the current study, the intravascular solute transit time ( $\sim 3$  s) is small compared to the imaging time periods (75–80 s) and to the time constant  $1/\alpha_0$  for solute extravasation (10–100 s). Thus, the assumption of fast flow is justified, and models that do not make this assumption (2CXM and ATH) would likely be less well-suited for analyzing the data. In actual tissues, the transit times can be nearly an order-of-magnitude larger, depending on the tissue and the size of an image pixel, and use of the more complex models that explicitly consider the intravascular transit time can be justified. For most cases that we analyzed, the intravascular solute transit time was also lower than the extravascular transit time  $PS/V_e$  (80–8000 s), which explains why the unidirectional transport model was sufficient in these cases. Neglecting solute return in the blind algorithm or with Patlak analysis both consistently predicted lower permeabilities than when solute return was allowed, a finding that has been reported by others (Cramer and Larsson, 2014; Oosterbroek et al., 2015).

Previous studies of blind deconvolution have relied extensively on multichannel approaches using the same bidirectional model that we applied here (Fluckiger et al., 2009; Schabel et al., 2010; Yang et al., 2007). In these studies, imaging data from two or more ROIs or from one ROI and one reference region are used to bypass the need for direct measurement of the AIF. Multichannel deconvolution assumes that the AIF to the different ROIs are the same, or differ at most by an unknown delay time. In contrast, our algorithms are single-channel ones, and rely only on the imaging data from a single ROI. Single-channel blind deconvolution subjects the vascular input to physiological constraints (e.g., non-negativity) to promote convergence of the algorithm (Grüner and Tact, 2006; Tact et al., 2012; Tact et al., 2015). Previous work by Tact and co-workers compared blind and non-blind deconvolution using two transport models (ATH and 2CXM) (Tact et al., 2015). This study found that blind approaches fit imaging data better than non-blind ones did and yielded more physiological values of the perfusion parameters.

#### 4.3. Practical considerations

Although the blind algorithm was essentially perfect when applied to noise-free data, clinical imaging data are inherently noisy, which can lead to errors in the predicted permeabilities. One way to compensate for low signal-to-noise levels would be to increase both the imaging time period  $T$  and the averaging window  $\Delta T$ . A complementary solution to the issue of noisy data would be to bin the imaging signal across neighboring voxels (similar to a spatial averaging filter). Regardless of the exact strategy used, our data indicate that  $SNR$  of 40 is sufficient for good performance of the permeability algorithm.

A second source of error stemmed from the assumption that the vascular signal decays to zero by the end of the imaging time. In practice, injected solute is never completely cleared from the bloodstream during imaging (Parker et al., 2006). Our results suggest that keeping the residual vascular signal to at most 2% of the maximum will lead to moderate overestimate of  $\alpha$ . Depending on the imaging protocol, this level of residual solute may be achievable with long imaging times on the order of 10–15 min. For example, the population-averaged MRI-derived AIFs from Parker et al. display a residual of 6.3% after 6 min and, when extrapolated using the fitted parameters, < 2% after 13 min (Parker et al., 2006). Similarly, the CT-derived AIF from Dankbaar et al. shows a residual of 3.5% after 3 min (Dankbaar et al., 2008a). We acknowledge that for particular combinations of imaging modality, injection protocol, tissue analyzed, etc., a 2% maximum residual may not be achievable. For these cases, it should be possible to modify the algorithm to target a non-zero long-term vascular signal and slope, although these values would need to be obtained from prior knowledge of the solute's pharmacokinetics. Other sources of error, such as that resulting from discrete sampling of the tissue intensity, appear to be less significant.

Although our simulations only considered intensity-time data that spanned at most 80 s, they can be generalized to longer imaging periods by scaling the time. In principle, the blind algorithm should perform equivalently when the time period is increased by a constant factor and the permeability is decreased by the same factor. To test this idea, we applied the blind algorithm to simulated imaging data from a tissue cylinder with 15  $\mu\text{m}$  intercapillary spacing,  $\alpha_0 = 0.01/\text{s}$ , a solute delay time of 5 s, and an imaging period of  $T = 355$  s (i.e., 350 s plus the delay). This case represents a fivefold time-scaled analog of the one with  $\alpha_0 = 0.05/\text{s}$  and  $T = 75$  s, which could be accurately analyzed with the blind algorithm and a bidirectional model (Fig. 5). Indeed, for the time-extended case, the predicted  $\alpha$  (median 0.0122/s, 90% confidence interval 0.0120/s–0.0125/s) and  $k$  (median 0.00123/s, 90% confidence interval 0.00119/s–0.00127/s) matched the theoretical values of 0.01/s and 0.00125/s well. Long imaging time periods, large permeabilities, and large vascular spaces benefit from the use of a bidirectional versus a unidirectional model. In this light, extended imaging data from tumors would be a natural first test for the blind algorithm developed in this study.

Strictly speaking, blind algorithms with linear transport models can only yield ratios of transport parameters (e.g.,  $PS/V_p$  rather than  $PS$  or  $V_p$  separately). To obtain absolute values of these parameters, one measurement from the AIF (e.g., the value of the AIF at the last time-point, or the time-integral of the AIF) is required (Riabkov and Di Bella, 2002). This requirement holds for our algorithms and for those developed by others.

Overall, the blind algorithm was fast, typically requiring at most a few seconds to complete the permeability calculations on a standard PC workstation with a precision of  $5 \times 10^{-5}/\text{s}$ . For a typical clinical image slice resolution of  $128 \times 128$  pixels, it should be possible to generate a permeability map within several minutes with a precision of 0.001/s, which corresponds to a precision of  $\sim 10^{-7}$  cm/s for the solute permeability coefficient, sufficient for most applications.

### 5. Conclusions

The algorithm described in this study enables one to map vascular permeabilities from time-lapse imaging data without knowledge of an arterial input function. Our results indicate that the errors associated with this blind deconvolution of imaging data can be surprisingly small under clinically acceptable imaging settings (signal-to-noise ratio of 40, total imaging time of 60–80 s, and imaging frequency of 1 Hz). Most importantly, this algorithm outperforms the standard Patlak analysis, which requires measurement of an AIF and is thus vulnerable to solute delay and dispersion. Bidirectional transport models did not show a clear advantage over simpler, unidirectional models, except for the combination of high permeability and low intercapillary spacing. Incorporation of the blind algorithm into current commercially available software for vascular imaging should be straightforward, and should increase the accuracy of permeability maps for the diagnosis and

treatment of pathologies that involve breakdown of the vascular barrier.

Supplementary data to this article can be found online at <https://doi.org/10.1016/j.mvr.2020.104102>.

### Declaration of competing interest

The authors declare no conflicts of interest.

### Acknowledgments

We thank Dr. Dimitris Mitsouras (Brigham and Women’s Hospital) and Drs. Hernán Jara and Asim Mian (Boston University School of Medicine) for helpful discussions. This work was funded through a grant from the Boston University Biomedical Engineering and Brigham and Women’s Hospital Partnership Program.

### Appendix A

#### Justification of blind deconvolution algorithm

This Appendix provides the mathematical basis for the algorithm developed in this study to obtain the true vascular permeability constants  $\alpha_0$  and  $k_0$ . The analysis assumes that the vascular signal  $I_v(t)$  rises from a value of zero at time  $t = 0$ , reaches a maximum, and decreases back to zero by time  $t = T$  (the final time point).

The predicted vascular signal in Eq. (6) satisfies the following solute transport equation:

$$\frac{dI}{dt} = \frac{d\tilde{I}_v}{dt} + \alpha\tilde{I}_v - k(I - \tilde{I}_v) \tag{8}$$

Equating Eqs. (3) and (8) at  $t = T$  yields:

$$\left. \frac{d\tilde{I}_v}{dt} \right|_{t=T} = (k - k_0)I(T) - (\alpha + k)\tilde{I}_v(T) \tag{9}$$

Evaluating Eq. (6) at  $t = T$ , substituting into Eq. (9), and integrating by parts yield:

$$\begin{aligned} \left. \frac{d\tilde{I}_v}{dt} \right|_{t=T} &= (k - k_0)I(T) - (\alpha + k)I(T) + \alpha(\alpha + k)e^{-(\alpha+k)T} \int_0^T e^{(\alpha+k)t} I(t) dt \\ &= (k - k_0)I(T) - kI(T) - \alpha e^{-(\alpha+k)T} \int_0^T e^{(\alpha+k)t} \frac{dI}{dt} dt \\ &= -k_0I(T) - \alpha e^{-(\alpha+k)T} \int_0^T e^{(\alpha+k)t} \left[ \frac{dI_v}{dt} + \alpha_0 I_v - k_0(I - I_v) \right] dt \\ &= -k_0 \left[ I(T) - \alpha e^{-(\alpha+k)T} \int_0^T e^{(\alpha+k)t} I(t) dt \right] + \alpha(\alpha - \alpha_0 + k - k_0) e^{-(\alpha+k)T} \int_0^T e^{(\alpha+k)t} I_v(t) dt \\ &= -k_0\tilde{I}_v(T) + \alpha(\alpha - \alpha_0 + k - k_0) e^{-(\alpha+k)T} \int_0^T e^{(\alpha+k)t} I_v(t) dt \end{aligned} \tag{10}$$

Both  $I(T)$  and the integral in the last line of Eq. (10) are non-zero. Thus, Eqs. (9) and (10) show that the long-term value and slope of  $\tilde{I}_v(t; \alpha, k)$  can simultaneously equal zero only when  $\alpha = \alpha_0$  and  $k = k_0$ .

Eqs. (9) and (10) also indicate that, for small deviations about  $\alpha = \alpha_0$  and  $k = k_0$ , both  $d\tilde{I}_v/dt|_{t=T}$  and  $\tilde{I}_v(T)$  will be linear functions of  $\alpha - \alpha_0$  and  $k - k_0$ . This finding of linear response implies that our “staircase” search strategy will locally converge to the correct values of  $\alpha_0$  and  $k_0$ . Global convergence is not guaranteed, however, and must be checked numerically for each set of solute intensity data.

#### Expressions for vascular input and AIF

For the analytical two-compartment models used in Figs. 2, 3, 4A, and 4B, the vascular input consisted of a single bolus:

$$I_v(t) = (t^2/\tau^2) e^{1-t^2/\tau^2} \tag{11}$$

with  $\tau = 10$  s.

For the analytical two-compartment models used in Fig. 4C, the vascular input consisted of an initial bolus, a smaller secondary peak, and a residual:

$$I_v(t) = (t^2/\tau^2)e^{1-t^2/\tau^2} + 0.2H(t-\tau_1)\left(\frac{t-\tau_1}{\tau}\right)^2 e^{1-(t-\tau_1)^2/\tau^2} + \delta\left(1 - e^{-t^2/\tau^2}\right)e^{-t/\tau_2} \quad (12)$$

Here,  $H(t)$  is the Heaviside step function,  $\tau = 10$  s,  $\tau_1 = 20$  s, and  $\tau_2 = 40$  s. The parameter  $\delta$  represents the amount of residual vascular input and ranged up to 0.2 (equivalent to a residual signal at  $t = 70$  s of  $\sim 2\%$  of the maximum vascular input). The middle term represents solute recirculation and begins at a time  $\tau_1$  relative to the initial bolus.

For the finite-element models used in Figs. 5, S1, and S2, the vascular input consisted of an initial bolus, a smaller secondary peak, and a residual:

$$I_v(t) = 0 \text{ for } t \leq \tau_{\text{delay}}$$

$$I_v(t) = \left(\left(t - \tau_{\text{delay}}\right)^2 / \tau^2\right) e^{1 - (t - \tau_{\text{delay}})^2 / \tau^2} + 0.2H(t - \tau_{\text{delay}} - \tau_1)\left(\frac{t - \tau_{\text{delay}} - \tau_1}{\tau}\right)^2 e^{1 - (t - \tau_{\text{delay}} - \tau_1)^2 / \tau^2} + 0.06\left(1 - e^{-(t - \tau_{\text{delay}})^2 / \tau^2}\right) e^{-(t - \tau_{\text{delay}}) / \tau_2} \text{ for } t \geq \tau_{\text{delay}} \quad (13)$$

with  $\tau = 10$  s,  $\tau_1 = 20$  s, and  $\tau_2 = 40$  s. The parameter  $\tau_{\text{delay}}$  represents the time between the start of the AIF and  $I_v$ , and was either 5 or 10 s. In Patlak analysis of imaging data from finite-element models (Fig. 5A), the AIF consisted of narrower boluses, along with a residual:

$$AIF(t) = (10 \text{ sec} / \tau) \left[ (t^2 / \tau^2) e^{1 - t^2 / \tau^2} + 0.2H(t - \tau_1) \left( \frac{t - \tau_1}{\tau} \right)^2 e^{1 - (t - \tau_1)^2 / \tau^2} \right] + 0.06 \left( 1 - e^{-t^2 / \tau^2} \right) e^{-t / \tau_2} \quad (14)$$

with  $\tau = 6.7$  s,  $\tau_1 = 20$  s, and  $\tau_2 = 40$  s. Here, the boluses in the AIF were assumed to be less-dispersed versions of the ones in  $I_v$ . Because the AIF was not time-shifted, the peaks of the corresponding boluses in the AIF and  $I_v$  differed in time by approximately  $\tau_{\text{delay}}$ .

## References

- Brix, G., Bahner, M.L., Hoffmann, U., Horvath, A., Schreiber, W., 1999. Regional blood flow, capillary permeability, and compartmental volumes: measurement with dynamic CT: initial experience. *Radiology*. 210, 269–276.
- Calamante, F., Gadian, D.G., Connelly, A., 2000. Delay and dispersion effects in dynamic susceptibility contrast MRI: simulations using singular value decomposition. *Magn. Reson. Med.* 44, 466–473.
- Chen, J.J., Smith, M.R., Frayne, R., Partial volume effect in quantitative magnetic resonance perfusion imaging. *Proceedings of the 26th Annual International Conference of the IEEE EMBS. IEEE, San Francisco, CA, 2004*, pp. 1132–1135.
- Cramer, S.P., Larsson, H.B.W., 2014. Accurate determination of blood-brain barrier permeability using dynamic contrast-enhanced T1-weighted MRI: a simulation and *in vivo* study on healthy subjects and multiple sclerosis patients. *J. Cereb. Blood Flow Metab.* 34, 1655–1665.
- Cuenod, C.A., Balvay, D., 2013. Perfusion and vascular permeability: basic concepts and measurement in DCE-CT and DCE-MRI. *Diagn. Interv. Imaging*. 94, 1187–1204.
- Dankbaar, J.W., Hom, J., Schneider, T., Cheng, S.-C., Lau, B.C., van der Schaaf, I., Virmani, S., Pohlman, S., Dillon, W.P., Wintermark, M., 2008a. Accuracy and anatomical coverage of perfusion CT assessment of the blood-brain barrier permeability: one bolus versus two boluses. *Cerebrovasc. Dis.* 26, 600–605.
- Dankbaar, J.W., Hom, J., Schneider, T., Cheng, S.-C., Lau, B.C., van der Schaaf, I., Virmani, S., Pohlman, S., Dillon, W.P., Wintermark, M., 2008b. Dynamic perfusion CT assessment of the blood-brain barrier permeability: first pass versus delayed acquisition. *Am. J. Neuroradiol.* 29, 1671–1676.
- Feng, D., Wong, K.-P., Wu, C.-M., Siu, W.-C., 1997. A technique for extracting physiological parameters and the required input function simultaneously from PET image measurements: theory and simulation study. *IEEE Trans. Inf. Technol. Biomed.* 1, 243–254.
- Fish, D.A., Brinicombe, A.M., Pike, E.R., Walker, J.G., 1995. Blind deconvolution by means of the Richardson-Lucy algorithm. *J. Opt. Soc. Am. A*. 12, 58–65.
- Fluckiger, J.U., Schabel, M.C., DiBella, E.V.R., 2009. Model-based blind estimation of kinetic parameters in dynamic contrast enhanced (DCE)-MRI. *Magn. Reson. Med.* 62, 1477–1486.
- Goresky, C.A., Ziegler, W.H., Bach, G.G., 1970. Capillary exchange modeling. Barrier-limited and flow-limited distribution. *Circ. Res.* 27, 739–764.
- Gravel, P., Beaudoin, G., De Guise, J.A., 2004. A method for modeling noise in medical images. *IEEE Trans. Med. Imaging* 23, 1221–1232.
- Grüner, R., Taxt, T., 2006. Iterative blind deconvolution in magnetic resonance brain perfusion imaging. *Magn. Reson. Med.* 55, 805–815.
- Hom, J., Dankbaar, J.W., Schneider, T., Cheng, S.-C., Bredno, J., Wintermark, M., 2009. Optimal duration of acquisition for dynamic perfusion CT assessment of blood-brain barrier permeability using the Patlak model. *Am. J. Neuroradiol.* 30, 1366–1370.
- Hom, J., Dankbaar, J.W., Soares, B.P., Schneider, T., Cheng, S.-C., Bredno, J., Lau, B.C., Smith, W., Dillon, W.P., Wintermark, M., 2011. Blood-brain barrier permeability assessed by perfusion CT predicts symptomatic hemorrhagic transformation and malignant edema in acute ischemic stroke. *Am. J. Neuroradiol.* 32, 41–48.
- Huxley, V.H., Curry, F.E., Adamson, R.H., 1987. Quantitative fluorescence microscopy on single capillaries:  $\alpha$ -lactalbumin transport. *Am. J. Physiol.* 252, H188–H197.
- Karakatsanis, N.A., Lodge, M.A., Tahari, A.K., Zhou, Y., Wahl, R.L., Rahmim, A., 2013. Dynamic whole-body PET parametric imaging: I. concept, acquisition protocol optimization and clinical application. *Phys. Med. Biol.* 58, 7391–7418.
- Karakatsanis, N.A., Zhou, Y., Lodge, M.A., Casey, M.E., Wahl, R.L., Zaidi, H., Rahmim, A., 2015. Generalized whole-body Patlak parametric imaging for enhanced quantification in clinical PET. *Phys. Med. Biol.* 60, 8643–8673.
- Koh, T.S., Bisdas, S., Koh, D.M., Thng, C.H., 2011. Fundamentals of tracer kinetics for dynamic contrast-enhanced MRI. *J. Magn. Reson. Imaging* 34, 1262–1276.
- Lin, E., Alessio, A., 2009. What are the basic concepts of temporal, contrast, and spatial resolution in cardiac CT? *J. Cardiovasc. Comput. Tomogr.* 3, 403–408.
- Logan, J., Fowler, J.S., Volkow, N.D., Wolf, A.P., Dewey, S.L., Schlyer, D.J., MacGregor, R.R., Hitzemann, R., Bendriem, B., Gatley, S.J., Christman, D.R., 1990. Graphical analysis of reversible radioligand binding from time-activity measurements applied to [ $^{11}\text{C}$ -methyl]-(-)-cocaine PET studies in human subjects. *J. Cereb. Blood Flow Metab.* 10, 740–747.
- Meyer, E., 1989. Simultaneous correction for tracer arrival delay and dispersion in CBF measurements by the  $\text{H}_2^{15}\text{O}$  autoradiographic method and dynamic PET. *J. Nucl. Med.* 30, 1069–1078.
- Oosterbroek, J., Bennis, E., Philippens, M.E.P., Raaijmakers, C.P.J., Viergever, M.A., de Jong, H.W.A.M., 2015. Comparison of DCE-CT models for quantitative evaluation of  $K^{\text{trans}}$  in larynx tumors. *Phys. Med. Biol.* 60, 3759–3773.
- Parker, G.J.M., Roberts, C., Macdonald, A., Buonaccorsi, G.A., Cheung, S., Buckley, D.L., Jackson, A., Watson, Y., Davies, K., Jayson, G.C., 2006. Experimentally-derived functional form for a population-averaged high-temporal-resolution arterial input function for dynamic contrast-enhanced MRI. *Magn. Reson. Med.* 56, 993–1000.
- Patlak, C.S., Blasberg, R.G., 1985. Graphical evaluation of blood-to-brain transfer constants from multiple-time uptake data. Generalizations. *J. Cereb. Blood Flow Metab.* 5, 584–590.
- Patlak, C.S., Blasberg, R.G., Fenstermacher, J.D., 1983. Graphical evaluation of blood-to-brain transfer constants from multiple-time uptake data. *J. Cereb. Blood Flow Metab.* 3, 1–7.
- Peters, A.M., 1994. Graphical analysis of dynamic data: the Patlak-Rutland plot. *Nucl. Med. Commun.* 15, 669–672.
- Riabkov, D.Y., Di Bella, E.V.R., 2002. Estimation of kinetic parameters without input functions: analysis of three methods for multichannel blind identification. *IEEE Trans. Biomed. Eng.* 49, 1318–1327.
- Schabel, M.C., Fluckiger, J.U., DiBella, E.V.R., 2010. A model-constrained Monte Carlo method for blind arterial input function estimation in dynamic contrast-enhanced MRI: I. Simulations. *Phys. Med. Biol.* 55, 4783–4806.
- Schneider, T., Hom, J., Bredno, J., Dankbaar, J.W., Cheng, S.-C., Wintermark, M., 2011. Delay correction for the assessment of blood-brain barrier permeability using first-pass dynamic perfusion CT. *Am. J. Neuroradiol.* 32, E134–E138.
- Sourbron, S.P., Buckley, D.L., 2011. On the scope and interpretation of the Tofts models for DCE-MRI. *Magn. Reson. Med.* 66, 735–745.
- Sourbron, S.P., Buckley, D.L., 2012. Tracer kinetic modelling in MRI: estimating perfusion and capillary permeability. *Phys. Med. Biol.* 57, R1–R33.
- Sourbron, S.P., Buckley, D.L., 2013. Classic models for dynamic contrast-enhanced MRI. *NMR Biomed.* 26, 1004–1027.
- St. Lawrence, K.S., Lee, T.-Y., 1998. An adiabatic approximation to the tissue homogeneity model for water exchange in the brain: I. Theoretical derivation. *J. Cereb. Blood Flow Metab.* 18, 1365–1377.

- Taxt, T., Jirfk, R., Rygh, C.B., Grüner, R., Bartoš, M., Andersen, E., Curry, F.-R., Reed, R. K., 2012. Single-channel blind estimation of arterial input function and tissue impulse response in DCE-MRI. *IEEE Trans. Biomed. Eng.* 59, 1012–1021.
- Taxt, T., Pavlin, T., Reed, R.K., Curry, F.-R., Andersen, E., Jirfk, R., 2015. Using single-channel blind deconvolution to choose the most realistic pharmacokinetic model in dynamic contrast-enhanced MR imaging. *Appl. Magn. Reson.* 46, 643–659.
- Truslow, J.G., Tien, J., 2013. Determination of vascular permeability coefficients under slow luminal filling. *Microvasc. Res.* 90, 117–120.
- Willats, L., Connelly, A., Calamante, F., 2006. Improved deconvolution of perfusion MRI data in the presence of bolus delay and dispersion. *Magn. Reson. Med.* 56, 146–156.
- Yang, C., Karczmar, G.S., Medved, M., Stadler, W.M., 2004. Estimating the arterial input function using two reference tissues in dynamic contrast-enhanced MRI studies: fundamental concepts and simulations. *Magn. Reson. Med.* 52, 1110–1117.
- Yang, C., Karczmar, G.S., Medved, M., Stadler, W.M., 2007. Multiple reference tissue method for contrast agent arterial input function estimation. *Magn. Reson. Med.* 58, 1266–1275.
- Yankeelov, T.E., Luci, J.J., Lepage, M., Li, R., Debusk, L., Lin, P.C., Price, R.R., Gore, J.C., 2005. Quantitative pharmacokinetic analysis of DCE-MRI data without an arterial input function: a reference region model. *Magn. Reson. Imaging* 23, 519–529.